Advanced Lab Course

Report for M.Phy.1601:

Development and Realization of Scientific Projects in Astro-/Geophysics

prepared by

Jan-Vincent Harre

Date: 13th August 2020

Supervisor: Dr. René Heller

Referee: Dr. René Heller

Contents

1. Introduction

A lot of publications in astronomy and astrophyiscs feature digitally created representations of stars. The actual colors of stars are often insignificant since only the astrophysical processes shown in illustrations are important. However, they can be helpful by relating i.e. temperatures of stars to colors, like in the Hertzsprung-Russel diagram [1, 2]. This is useful for different figures in papers, slides in science talks, and even artistic representations of stars. In some cases, the color of stars is important though, like for the color-induced displacement of binary stars [3] and the Rossiter-McLaughlin effect [4, 5]. Besides the scientific value of colors of stars, color-correct representations of stars are also a nice feature for public science communication.

Still, there is no uniform scale for digitized color codes of stars which leads to a greatly varying assignment of colors to even the same spectral types. Additionally, there is some partly misleading color information in the names of some stellar type groups, like red or white dwarfs.

In this report, a method of computing the colors of stars is introduced and described, and the digital color codes of main sequence stars are computed.

2. Methods

2.1. Stellar model spectra

Pre-computed model spectra were used as stellar input spectra in the calculations of the color codes. These spectra contain information on the flux densities as a function of wavelength of the light. Publicly available[1] PHOENIX spectra from Husser et al. [6] in the effective temperature range from $2300\,\text{K} \leq T_{\text{eff}} \leq 12,000\,\text{K}$ were used for the calculations. Spectra with surface gravity values of $0 \leq \log(g) \leq 6$, with g in units of $\text{cm}\,\text{s}^{-2}$, and metallicities of $[\text{Fe/H}] \in \{0, -1, -2\}$ were used from this spectral library. Additionally, spectra for T_{eff} up to $15,000\,\text{K}$ were provided by courtesy of T. O. Husser in private communication. All spectra feature the same wavelength grid $(500\,\text{Å} \leq \lambda \leq 5.5\,\mu\text{m})$ and are given with a typical resolution of $R = \lambda/\Delta\lambda = 500,000$ in the optical regime.

These spectra were computed using version 16 of the PHOENIX software [7]. Each stellar atmosphere was represented by 64 layers and spherical symmetry of the stars was assumed. The assumption of local thermal equilibrium (LTE) was justified by the maximum effective temperatures of $12,000\,\text{K}$. More details can be found in Husser et al. [6].

For OB stars with effective temperatures in the range of $16,000\,\text{K} \leq T_{\text{eff}} \leq 55,000\,\text{K}$, TLUSTY models[2] of the BSTAR2006 grid of Lanz and Hubeny [8] and the OSTAR2002 grid of Lanz and Hubeny [9] were used. These models take the effects of non-LTE in plane-parallel, hydrostatic atmospheric layers into account. The differences in the color codes are very small across different stellar metallicities due to the very weak absorption lines of these hot stars. For this reason, only solar metallicity spectra were used in the analysis.

---

[1] http://phoenix.astro.physik.uni-goettingen.de
[2] http://tlusty.oca.eu/Tlusty2002/tlusty-frames-OS02.html

2.2. **Color codes and Matching functions**

The Python module `color_system.py`[3] was used to calculate the digital color codes for the model spectra as if they were perceived by the human eye. In order to compute a color code from a spectrum, this module uses data from so-called color matching functions (CMFs), which describe the perception of light by the cone cells in the human eye. Because of the high wavelength resolution of the used model stellar spectra, the latest values of the 2-degree XYZ CMFs[4], transformed from the 2006 CIE (International Commission on Illumination) 2-degree LMS (long-medium-short color space) cone fundamentals [10], were used. These CMFs come with a resolution of one data point per Å. The resolution of the synthetic stellar spectra was degraded to the same wavelength resolution.

In Fig. 2.1 one can see the CMFs in blue, green and red together with two example spectra, one of which is a black body of 2500 K (black line) and the other one being a PHOENIX spectrum for $T_{\text{eff}} = 2500$ K, $\log(g) = 5$, and [Fe/H] $= 0$. Both spectra are normalized to a value of one which can be seen in the inset. The visible difference between the flux of the PHOENIX spectrum and the black body spectrum suggests a visible color difference between the two spectra. The difference comes from the presence of strong molecular absorption bands in the stellar spectrum. The surface gravity value of $\log(g) = 5$ was chosen since it is around the main sequence of stars.

2.3. **Spectral typing**

The PHOENIX spectra do not give information about spectral types (SpT) of the simulated stars, although empirical relationships can be used to relate the PHOENIX spectra with a SpT. To simplify the choice of an appropriate color representation for a given SpT, one of the goals was to create a suitable look-up table for astronomers that is astrophysically motivated.

For this, the spectral types of main-sequence stars were matched with the corresponding T_{eff} and $\log(g)$ values from the library of PHOENIX and TLUSTY models. First, Table 5 of Pecaut and Mamajek [12] was used to match T_{eff} from the synthetic models with observed spectral types of stars. These authors used a weighting scheme of a large sample of standard main-sequence stars from the literature to infer a T_{eff}-SpT relation for $T_{\text{eff}} \leq 34,000$ K. Stellar surface gravities were not provided.

---

[3]https://scipython.com/blog/converting-a-spectrum-to-a-colour
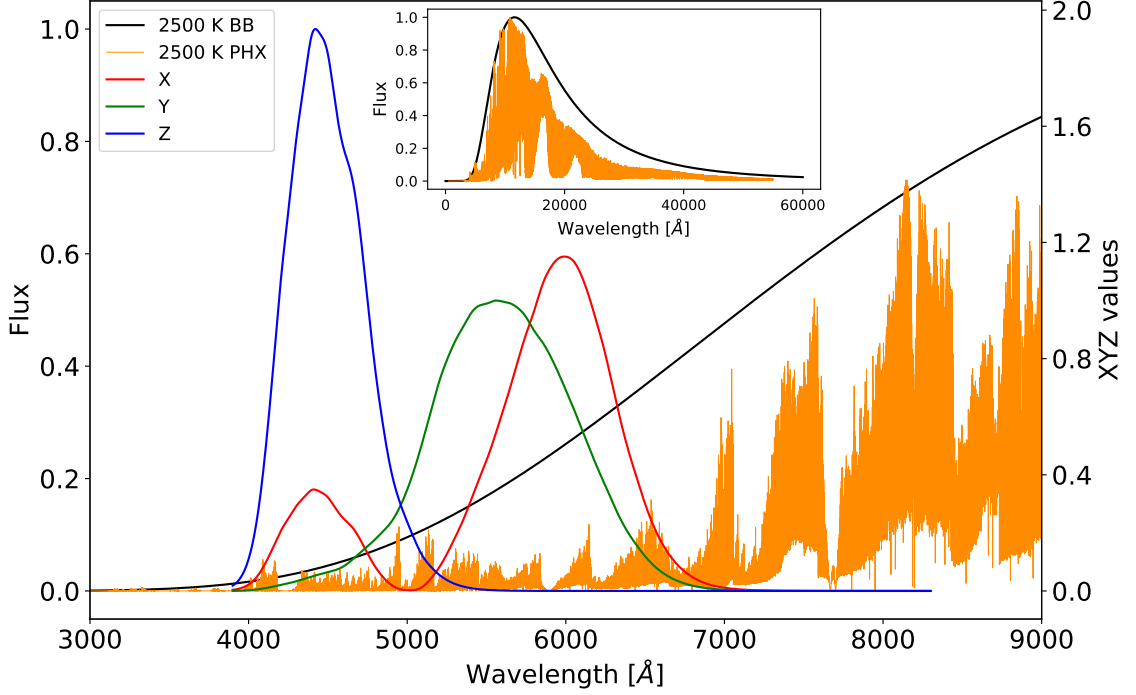[4]http://cvrl.ucl.ac.uk

Figure 2.1.: Comparison of a black body spectrum (labeled BB, black solid line) and a PHOENIX spectrum of a main-sequence star (labeled PHX, orange line), both with an effective temperature of 2500 K. The color matching functions are shown as X, Y and Z in red, green and blue, respectively. The inset shows an extended coverage of the spectra up to 60,000 Å. Figure taken from Harre and Heller [11].

As an alternative, three intervals of $\log(g)$ based on the T_{eff}-$\log(g)$ relation were defined. These are derived from a sample of detached eclipsing stellar binaries [13]:

$$
\begin{aligned}
T_{\text{eff}} &\leq 3648\,\text{K} & \Rightarrow & & \log(g) &= 5.0 \\
3648\,\text{K} < T_{\text{eff}} &\leq 6152\,\text{K} & \Rightarrow & & \log(g) &= 4.5 \\
6152\,\text{K} < T_{\text{eff}} & & \Rightarrow & & \log(g) &= 4.0 & (2.1)
\end{aligned}
$$

For $T_{\text{eff}} > 34,000\,\text{K}$ we used Table 7 of Eker et al. [13] for the SpT-to-T_{eff} matching.

2.4. Limb darkening

Limb darkening is used for illustrations only in this report. A quadratic limb darkening is used in this occasion:

2. Methods

$$\frac{I(\mu)}{I(1)} = 1 - a(1-\mu) - b(1-\mu)^2 \ , \tag{2.2}$$

where $\mu = \cos(\gamma)$, γ is the angle between the line of sight and the normal to the stellar surface, I is the specific intensity, and (a, b) are the limb darkening coefficients. This model does not take chromatic effects into account, meaning the possible wavelength dependence of limb darkening. Limb darkening coefficients that reproduce the limb darkening as observed in the G filter of the Gaia mission [Table 2 in 14] are used. This was chosen because the Gaia G filter's response curve matches reasonably well with the response function of the human eye [15]. Since not every combination of [Fe/H], $\log(g)$ and T_{eff} as given in the PHOENIX data is available in the limb darkening coefficients data from Claret [14], interpolation is used to fill the gaps in the data. The interpolation is done by taking the average of the coefficients from the configuration from before and after the missing coefficient in the list. This is possible because the PHOENIX and limb darkening coefficients datasets are ordered in the same way. In technical terms, limb darkening is implemented into the computer code by first creating a two-dimensional array with 1001×1001 entries, each containing a sub-array with the respective RGB color triple values of the star. Each RGB triple entry corresponded to a radial distance from the stellar enter. Using the relation $\mu = \sqrt{1 - r^2}$ [16], with $0 \leq r \leq 1$ being the radial distance from the star disk in units of stellar radii, each entry in the color array was multiplied with the corresponding intensity of the qudratic limb darkening in Eq. (2.2) law to obtain the radial limb darkening profile.

3. Results

3.1. Digital color codes

In Table 3.1, the RGB (column 2) and Hexadecimal (Hex) (column 3) color codes of black bodies with $2300 \leq T_{\text{eff}} \leq 12,000\,\text{K}$ are shown. This temperature range was chosen since it resembles the temperature range of the publicly available PHOENIX model spectra. The colors were computed as if the black body radiators were in space without any medium in the line of sight from the observer. In Table 3.2, the RGB and Hex color codes computed from the PHOENIX model spectra are shown for the temperature range from $2300 \leq T_{\text{eff}} \leq 15,000\,\text{K}$. Tables 3.3 and 3.4 show the RGB and Hex color codes as computed from the PHOENIX spectra for $2300 \leq T_{\text{eff}} \leq 12,000\,\text{K}$. Since the difference in color of stars with $T_{\text{eff}} > 12,000\,\text{K}$ is small, Tables 3.2 - 3.4 are restricted to the temperatures available in the PHOENIX model grid. Table 3.2, for $[\text{Fe/H}] = 0$, contains color codes for 847 PHOENIX spectra; Table 3.3 and its 846 entries refer to $[\text{Fe/H}] = -1$; and Table 3.4 is a list of 848 PHOENIX spectra assuming $[\text{Fe/H}] = -2$. The full tables are available at *zenodo.org*[1]. Table A.1 is a look-up table for the color codes of stars of a given spectral type and contains color codes computed from both the PHOENIX and the TLUSTY models with effective temperatures up to 55,000 K.

In Figure 3.1 the computed color codes from Table 3.2 are shown for several spectral types, representing the stellar main sequence, on the color wheel. Color codes were first computed using the PHOENIX and TLUSTY spectra and then a selection of spectral types were marked in the color wheel in steps of about half a spectral class between M9.5 to O1 (all of luminosity class V). From this, one can see that there are no true yellow, green, cyan, purple and pink stars. At the lowest temperatures, the main sequence begins with orange stars of SpT M9.5, then continues to produce brighter and brighter stars across the K class until it reaches the white point with stars of SpT F9.5. Sun-like stars with SpT G2 are

---

[1]http://cvrl.ucl.ac.uk

Table 3.1.: RGB and Hex color codes of black bodies. Only a part of the whole table is shown.

T_{eff}	RGB	Hex
2300	1.0,0.409,0.078	#ff6813
2400	1.0,0.432,0.093	#ff6e17
2500	1.0,0.455,0.109	#ff731b
2600	1.0,0.476,0.126	#ff7920
2700	1.0,0.497,0.144	#ff7e24
2800	1.0,0.518,0.163	#ff8429
2900	1.0,0.537,0.182	#ff892e
3000	1.0,0.557,0.202	#ff8d33
3100	1.0,0.575,0.223	#ff9238
3200	1.0,0.593,0.244	#ff973e
3300	1.0,0.611,0.266	#ff9b43
3400	1.0,0.627,0.289	#ff9f49
3500	1.0,0.644,0.311	#ffa44f
...	...	...

Table 3.2.: RGB and Hex color codes of stars with solar metallicity ([Fe/H] = 0) as seen from space, computed using PHOENIX model spectra. Only a portion of the whole table is shown here.

T_{eff}	$\log(g)$	[Fe/H]	RGB	Hex
2300	3.0	0.0	1.0,0.615,0.292	#ff9c4a
2300	3.5	0.0	1.0,0.571,0.25	#ff913f
2300	4.0	0.0	1.0,0.539,0.211	#ff8935
2300	4.5	0.0	1.0,0.507,0.175	#ff812c
2300	5.0	0.0	1.0,0.491,0.144	#ff7d24
2300	5.5	0.0	1.0,0.435,0.098	#ff6e19
2300	6.0	0.0	1.0,0.393,0.076	#ff6413
2400	3.0	0.0	1.0,0.66,0.313	#ffa84f
2400	3.5	0.0	1.0,0.653,0.309	#ffa64e
2400	4.0	0.0	1.0,0.604,0.266	#ff9a43
2400	4.5	0.0	1.0,0.549,0.212	#ff8b36
2400	5.0	0.0	1.0,0.518,0.179	#ff842d
2400	5.5	0.0	1.0,0.484,0.137	#ff7b23
2400	6.0	0.0	1.0,0.434,0.098	#ff6e19
...	...	...	...	...

Table 3.3.: RGB and Hex color codes of stars with [Fe/H] = −1 as seen from space, computed using PHOENIX model spectra. Only a portion of the whole table is shown here.

T_{eff}	log(g)	[Fe/H]	RGB PHX	Hex PHX
2300	3.0	-1.0	1.0,0.752,0.303	#ffbf4d
2300	3.5	-1.0	1.0,0.637,0.213	#ffa236
2300	4.0	-1.0	1.0,0.559,0.151	#ff8e26
2300	4.5	-1.0	1.0,0.493,0.103	#ff7d1a
2300	5.0	-1.0	1.0,0.469,0.086	#ff7715
2300	5.5	-1.0	1.0,0.425,0.059	#ff6c0f
2300	6.0	-1.0	1.0,0.392,0.045	#ff640b
2400	3.0	-1.0	1.0,0.774,0.312	#ffc54f
2400	3.5	-1.0	1.0,0.671,0.232	#ffab3b
2400	4.0	-1.0	1.0,0.604,0.183	#ff992e
2400	4.5	-1.0	1.0,0.517,0.123	#ff831f
2400	5.0	-1.0	1.0,0.468,0.09	#ff7717
2400	5.5	-1.0	1.0,0.426,0.063	#ff6c0f
2400	6.0	-1.0	1.0,0.406,0.052	#ff670d
...	...	...	...	...

Table 3.4.: RGB and Hex color codes of stars with [Fe/H] = −2 as seen from space, computed using PHOENIX model spectra.

| T_{eff}	log(g)	[Fe/H]	RGB PHX Space	Hex PHX Space
2300	3.0	-2.0	1.0,0.525,0.082	#ff8514
2300	3.5	-2.0	1.0,0.48,0.067	#ff7a10
2300	4.0	-2.0	1.0,0.443,0.057	#ff710e
2300	4.5	-2.0	1.0,0.422,0.054	#ff6b0d
2300	5.0	-2.0	1.0,0.41,0.052	#ff680d
2300	5.5	-2.0	1.0,0.394,0.051	#ff640d
2300	6.0	-2.0	1.0,0.382,0.055	#ff610d
2400	3.0	-2.0	1.0,0.527,0.09	#ff8617
2400	3.5	-2.0	1.0,0.506,0.082	#ff8115
2400	4.0	-2.0	1.0,0.468,0.07	#ff7711
2400	4.5	-2.0	1.0,0.437,0.064	#ff6f10
2400	5.0	-2.0	1.0,0.417,0.062	#ff6a0f
2400	5.5	-2.0	1.0,0.406,0.061	#ff670f
2400	6.0	-2.0	1.0,0.394,0.065	#ff6410
...	...	...	...	...
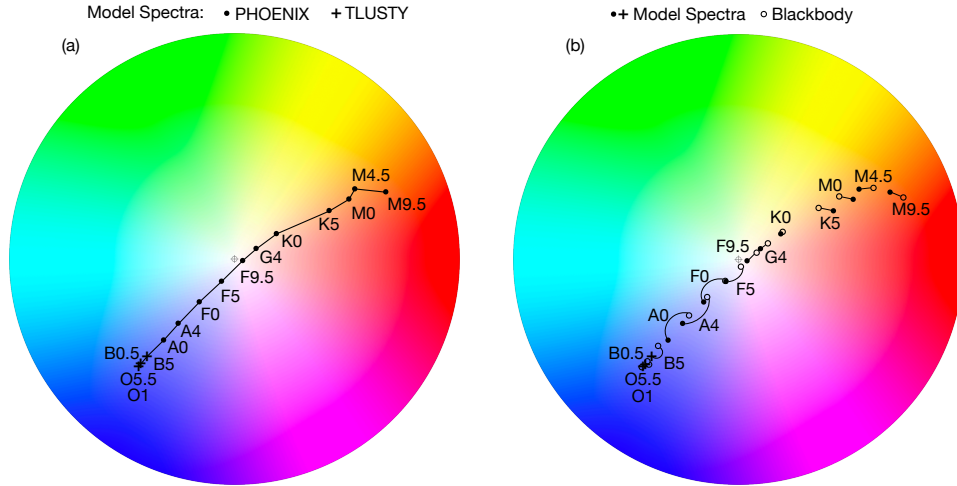
Figure 3.1.: (a) Main sequence stars in the color wheel. Colors are derived from synthetic stellar spectra. (b) Comparison of colors derived from synthetic spectra (filled circles) with colors calculated from black bodies of the corresponding effective temperatures (open circles). Spectral types are indicated along the curves. Figure by courtesy of René Heller [11].

slightly yellowish. Early-type stars of spectral classes A, B, and O tend to have ever more blue colors. For stars with spectral types earlier than about B5 the colors of increasingly hotter stars converge towards a blueish tone of RGB = (90,123,255). Figure 3.1 (b) shows the color difference between the model spectra and black bodies of the corresponding temperatures. It can be seen that for late spectral types the black body color is redder compared to the model spectra. This is only the case up to a spectral type between M4.5 and M0, where an inflection point is located. The color difference of spectral types earlier than this inflection point show for the model spectra a redder color compared to the black body colors. This trend reduces up to a second inflection point at a spectral type later than K0, from where on the black body colors appear redder again. The biggest color differences are present for spectral types of class A. For earlier spectral types, the color differences get smaller again.

3.2. Limb darkening

The effect of limb darkening is shown in Fig. 3.2 for a sun-like star with a temperature of 5700 K. The left panel has no limb darkening applied, while the right panel includes the quadratic limb darkening law. The quadratic limb darkening
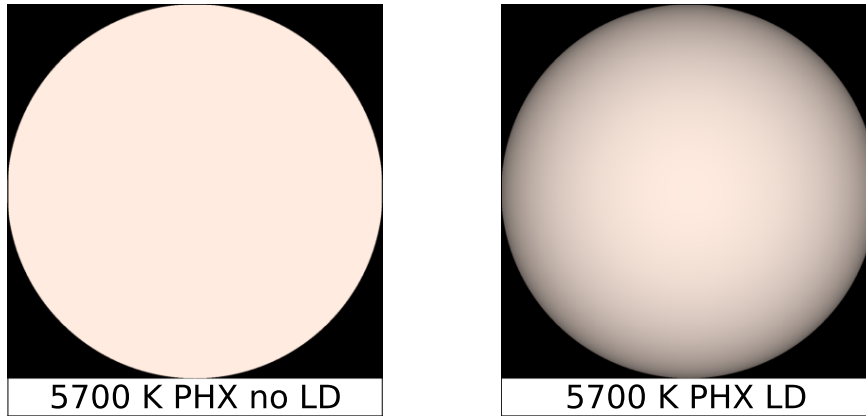
Figure 3.2.: Comparison of the same star with and without limb darkening. For the computation of the color we chose the PHOENIX spectrum of a sun-like star with $T_{\text{eff}} = 5700$ K, $\log(g) = 4.5$, and [Fe/H] $= 0$. Figure taken from Harre and Heller [11].

is implemented after the color calculation from the spectrum, so that also spectra of different types than stellar spectra can be analyzed. This means that the color codes from Tables 3.2 - 3.4 and Table A.1 represent the color of the center of each stellar disk. For each of the 105 stars listed in the look-up Table A.1, illustrations in portable document format (PDF, version 1.4) using the python plotting package `matplotlib` were generated. These illustrations are similar to the one in the right panel of Fig. 3.2.

3.3. Black bodies and stellar spectra

Examples of colors from the model spectra and black bodies are shown in Figure 3.3. The left column shows stellar disks of black bodies of different temperatures, while the right column shows stellar disks computed from PHOENIX model spectra. Quadratic limb darkening was applied to all stellar disks. The top row was calculated using spectra for effective temperatures of $2700\,\text{K}$, the middle row for $T_{\text{eff}} = 5200\,\text{K}$ and the bottom row for $T_{\text{eff}} = 8000\,\text{K}$.

For the $2700\,\text{K}$ spectra, one can see that the black body spectrum appears redder compared to the color computed using the corresponding PHOENIX spectrum. The black body color has lower G and B values, causing the darker, and in contrast redder, color of the stellar disk. The redness of the black body color could be one of the reasons for the name of so-called "red dwarfs". The $5200\,\text{K}$ spectra appear to be virtually the same. The differences in the RGB codes of both illustrations are 0 for

the R values, 0.001 for the G values and 0.003 for the B values. The 8000 K stellar disks show a greater color difference again. The black body appears to be lighter, which is caused by its higher R and G values compared to the PHOENIX spectrum color.

The display of model stars in Figure 3.4 shows a color- and size-correct comparison between main sequence stars of different spectral types. The colors were computed from PHOENIX and TLUSTY models and can also be seen in Table A.1. Quadratic limb darkening has been applied to these stellar disks. The stellar radii are scaled according to Eker et al. [13] for main-sequence stars of the respective spectral types. Extinction caused by media between the observer and the stars was neglected.
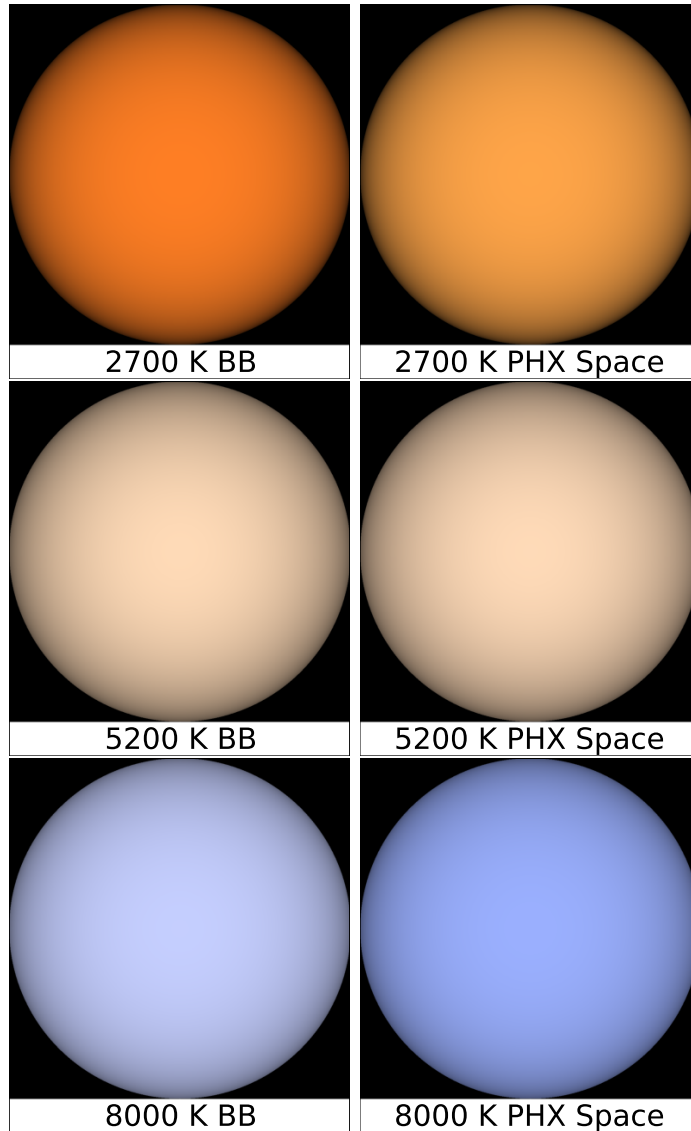
Figure 3.3.: Color representations of three stars with T_{eff} = 2700 K (top), T_{eff} = 5200 K (center), and T_{eff} = 8000 K (bottom). Colors in the left column are computed from a black body and colors in the right column from the PHOENIX spectra. For the PHOENIX models, solar metallicity ([Fe/H] = 0) was assumed as well as $\log(g)$ = 5.0, $\log(g)$ = 4.5, and $\log(g)$ = 4.0, respectively. The corresponding color codes are listed in Table 3.2. Quadratic limb darkening is modeled on top of the stellar disk. Perception of the colors (and their differences) depends on the monitor or print as well as on the individual vision abilities of the viewer. Figure taken from Harre and Heller [11].

| M9 | M2 | K2 | G2 | F2 | A2 | B2 | O2 |
| 2300 K | 3600 K | 5000 K | 5800 K | 6800 K | 8800 K | 21,000 K | 52,500 K |
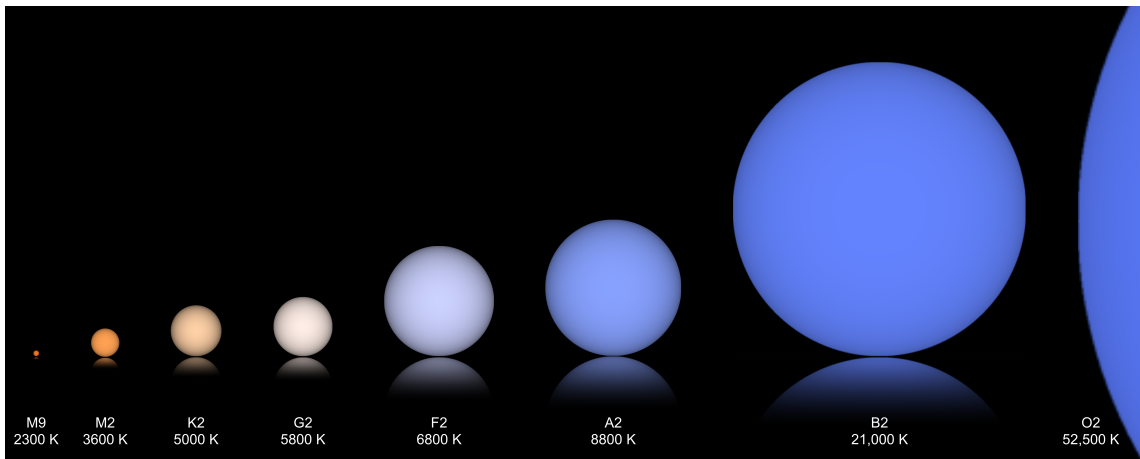
Figure 3.4.: Selection of main-sequence stars with proper limb darkening, radii to scale and colors as computed in this report. All stars are of luminosity class V. From a human-perception point of view the plausibility of such an illustration is limited because the hottest stars (spectral type O) can be millions or billions times more luminous than the coolest stars of (spectral type M). The effect of brightness is neglected here. Figure by courtesy of René Heller [11].

4. Discussion

The computed color codes do not contain information about the brightness of stars. Only hue and saturation are regarded. If stellar brightness was to be included, additional assumptions would need to be made, like their luminosity. The information about the luminosity of stars could be retrieved from mass-luminosity relations, this would require information about the stellar masses, which are not given in the used models. To get the masses of stars, ages would have to be assumed to match the given effective temperatures and surface gravities between the pre-computed models for the spectra and stellar evolution models. Moreover, to compute the apparent brightnesses, distances would need to be assumed.

Illustrations of stellar disks in this report make use of the quadratic limb darkening law. However, only achromatic effects are taken into account. This means that the illustrations are not necessarily perfectly correct, since there are chromatic effects, which have also been observed for the Sun [17]. A chromatic variations towards the limb of the stellar disk are expected because of the wavelength dependence of stellar limb darkening. Still, the computed color codes are not affected by this, since limb darkening is, in this report, only used for illustration purposes.

The used CMFs had a maximum resolution of one datapoint per Å, which limits the accuracy of the color calculations. This means that CMFs with a higher resolution could yield more accurate results. For this purpose, the effect of CMFs with a lower resoltion was tested. The resolution of the CMFs was artificially degraded by a factor of 2 by removing the values for every second wavelength. This does also degrade the resolution of the spectra to the same level because of the implementation of it. For the black body color codes, this resulted in a color code difference on the permille level which would probably not be noticeable to an observer. For the color codes of the PHEONIX spectra, the situation was different. For main sequence stars the color difference was always below 1% between the two CMF resolutions. In general, for stars with $T_{\text{eff}} > 3000\,\text{K}$, the color code difference was $< 1\%$ in all cases. For the most extreme cases of very low surface gravities with $\log(g) = 0$, the

4. Discussion

color differences for the G values were up to 2.5% for $2600\,\text{K} < T_\text{eff} < 3000\,\text{K}$ and up to 8% for $2300\,\text{K} < T_\text{eff} < 2600\,\text{K}$. The R and B values showed differences on a 1% level for these stars. This means that the computed color codes are accurate to one percent for effective temperatures below $3000\,\text{K}$ and accurate to one permille for effective temperatures above $3000\,\text{K}$ for main sequence stars.

CMFs are usually derived from a series of experiments with test persons. The results of different test series are different, but similar [18]. This is why a different set of CMFs would result in similar color codes. However, colors are perceived differently by different people and the biggest difference in the perception of the colors computed in this report stems from the nonidentical color display ability of different monitors and printers.

All of the colors computed in this report are calculated as seen from space without any media between the observer and the stars. This means that no extinction or other effects influencing the light coming from the stars were taken into account. If the stars were observed from the ground, the colors could look different caused by different effects in the Earth atmsopher like scattering of the light, scintillation and the presence of carbon black dust and other particles [19, Chapter 19]. However, the effects of the transmission of light through the atmosphere were tested. This was done by creating an absorption spectrum of the Earth's atmosphere using data from the HITRAN[1] database [20]. Every molecule and isotopologue listed in the database, except for the CO_2 isotopologues $^{18}C^{13}C^{17}O$ and $^{13}C^{17}O_2$, was used in the generation of the absorption spectrum. The yielded spectrum was normalized and degraded to the $1\,\text{Å}$ resolution of the CMFs and then multiplied to the spectra. The resulting color differences were always on the one permille level. The other listed effects would probably lead to greater differences in the color codes.

The computed black body color codes can be safely used for illustrations of DC white dwarfs, since the spectra of these stars are very close to spectra of black body radiators. The spectra of DC white dwarfs show basically no absorption lines [21, 22]. White dwarfs of this spectral type with effective temperatures below $5000\,\text{K}$ actually look slightly orange, comparable to the color in Table A.1 for a spectral type of K2.5V. A current example is the star of the recently discovered transiting exoplanet candidate WD 1856+534 b [23]. To a human observer. this DC white dwarf would have a pale orange color with a given temperature of $T_\text{eff} = 4710 \pm 60\,\text{K}$.

---

[1]https://hitran.org

5. Conclusion

In this report, the colors of pre-computed model spectra were determined using color matching functions which represent the color perception of the human eye. These determined colors differ in most of the cases considerably from the determined colors of the spectra of black body radiators.

In the case of a main sequence red dwarf with a temperature of $T_{\text{eff}} = 2300\,\text{K}$ and spectral type M9.5V, the color difference between a black body radiator and the PHOENIX spectrum is substantial with the difference being 0.082 in the G channel and 0.066 in the B channel. These differences lead to a much redder color of the black body spectrum compared to the PHOENIX spectrum. This could be an explanation for the name "red dwarf", even though these stars are actually more orange. The colors computed from black body and PHOENIX spectra differ only slightly, if at all, for stars of spectral type K1V to K0V. The colors are virtually the same in this spectral type range. This is different for early type main sequence stars. The colors computed from PHOENIX spectra appear more blue in contrast to the corresponding black body spectra with the difference getting smaller for even hotter early type stars.

The transmission of stellar light through the Earth's atmosphere is on the per-mille level and negligible for the color computation regarding only absorption from molecules. Other effects on the stellar light in the atmosphere probably have stronger influences on the colors of stars.

The color codes presented in this report, in combination with the used quadratic limb darkening law, can be used to create color-correct, realistic illustrations of main sequence stars with achromatic limb darkening. The written computer code, `Spec2Col.py`, is freely available and can be used to calculate the color codes for any type of input spectrum.

A. Appendix

Table A.1.: RGB and Hex color codes of solar metallicity main sequence stars for spectral types (SpT) M9.5V - O1V.

SpT	T_{eff}	$\log(g)$	RGB	Hex	
M9.5V	2300	5.0	1.0,0.491,0.144	#ff7d24	●
M9V	2400	5.0	1.0,0.518,0.179	#ff842d	●
M8V	2500	5.0	1.0,0.542,0.202	#ff8a33	●
M7.5V	2600	5.0	1.0,0.607,0.255	#ff9a41	●
M6.5V	2700	5.0	1.0,0.648,0.286	#ffa548	●
M6V	2800	5.0	1.0,0.649,0.285	#ffa548	●
M6V	2900	5.0	1.0,0.644,0.285	#ffa448	●
M5.5V	3000	5.0	1.0,0.641,0.289	#ffa349	●
M4.5V	3100	5.0	1.0,0.638,0.293	#ffa24a	●
M4V	3200	5.0	1.0,0.638,0.3	#ffa24c	●
M3.5V	3300	5.0	1.0,0.638,0.308	#ffa24e	●
M3V	3400	5.0	1.0,0.638,0.315	#ffa250	●
M2.5V	3500	5.0	1.0,0.637,0.322	#ffa251	●
M2V	3600	5.0	1.0,0.635,0.327	#ffa153	●
M1V	3700	4.5	1.0,0.637,0.34	#ffa256	●
M0.5V	3800	4.5	1.0,0.635,0.346	#ffa158	●
M0V	3900	4.5	1.0,0.636,0.354	#ffa25a	●
K8V	4000	4.5	1.0,0.641,0.369	#ffa35e	●
K7V	4100	4.5	1.0,0.65,0.389	#ffa563	●
K6.5V	4200	4.5	1.0,0.662,0.411	#ffa868	●
K5.5V	4300	4.5	1.0,0.677,0.439	#ffac6f	●
K5V	4400	4.5	1.0,0.696,0.47	#ffb177	●
K4.5V	4500	4.5	1.0,0.717,0.501	#ffb67f	●
K4V	4600	4.5	1.0,0.739,0.533	#ffbc87	●
K3.5V	4700	4.5	1.0,0.761,0.565	#ffc18f	●
K3V	4800	4.5	1.0,0.781,0.595	#ffc797	●
K3V	4900	4.5	1.0,0.802,0.626	#ffcc9f	●
K2.5V	5000	4.5	1.0,0.821,0.657	#ffd1a7	●
K1.5V	5100	4.5	1.0,0.84,0.691	#ffd6b0	●
K1V	5200	4.5	1.0,0.857,0.722	#ffdab8	●

Table A.1.: *(continued)*

SpT	T_{eff}	$\log(g)$	RGB	Hex	
K0V	5300	4.5	1.0,0.872,0.753	#ffdec0	
G9V	5400	4.5	1.0,0.886,0.783	#ffe1c7	
G8V	5500	4.5	1.0,0.898,0.813	#ffe5cf	
G6V	5600	4.5	1.0,0.91,0.845	#ffe8d7	
G4V	5700	4.5	1.0,0.922,0.878	#ffebdf	
G2V	5800	4.5	1.0,0.931,0.905	#ffede6	
G1V	5900	4.5	1.0,0.94,0.931	#ffefed	
F9.5V	6000	4.5	1.0,0.951,0.967	#fff2f6	
F9V	6100	4.5	1.0,0.96,0.998	#fff4fe	
F8V	6200	4.0	0.955,0.931,1.0	#f3edff	
F6V	6300	4.0	0.922,0.908,1.0	#ebe7ff	
F6V	6400	4.0	0.896,0.891,1.0	#e4e3ff	
F5V	6500	4.0	0.869,0.871,1.0	#dddeff	
F4V	6600	4.0	0.844,0.855,1.0	#d7d9ff	
F3V	6700	4.0	0.823,0.84,1.0	#d1d6ff	
F2V	6800	4.0	0.802,0.826,1.0	#ccd2ff	
F2V	6900	4.0	0.782,0.812,1.0	#c7cfff	
F1V	7000	4.0	0.763,0.799,1.0	#c2cbff	
F0V	7200	4.0	0.725,0.773,1.0	#b8c5ff	
A9V	7400	4.0	0.692,0.75,1.0	#b0bfff	
A8V	7600	4.0	0.674,0.738,1.0	#abbcff	
A7V	7800	4.0	0.636,0.712,1.0	#a2b5ff	
A6V	8000	4.0	0.606,0.69,1.0	#9ab0ff	
A4V	8200	4.0	0.579,0.67,1.0	#93aaff	
A4V	8400	4.0	0.556,0.652,1.0	#8da6ff	
A3V	8600	4.0	0.546,0.645,1.0	#8ba4ff	
A2V	8800	4.0	0.531,0.634,1.0	#87a1ff	
A2V	9000	4.0	0.519,0.624,1.0	#849fff	
A1V	9200	4.0	0.508,0.616,1.0	#819dff	
A1V	9400	4.0	0.498,0.608,1.0	#7f9bff	
A0V	9600	4.0	0.49,0.601,1.0	#7d99ff	
A0V	9800	4.0	0.483,0.595,1.0	#7b97ff	
A0V	10000	4.0	0.477,0.59,1.0	#7996ff	
B9.5V	10200	4.0	0.472,0.586,1.0	#7895ff	
B9.5V	10400	4.0	0.467,0.582,1.0	#7794ff	
B9V	10600	4.0	0.463,0.578,1.0	#7693ff	
B9V	10800	4.0	0.459,0.575,1.0	#7592ff	
B9V	11000	4.0	0.456,0.572,1.0	#7491ff	
B9V	11200	4.0	0.453,0.57,1.0	#7391ff	
B9V	11400	4.0	0.451,0.567,1.0	#7290ff	
B9V	11600	4.0	0.45,0.566,1.0	#7290ff	

Table A.1.: *(continued)*

SpT	T_{eff}	$\log(g)$	RGB	Hex	
B8V	11800	4.0	0.448,0.564,1.0	#728fff	●
B8V	12000	4.0	0.446,0.562,1.0	#718fff	●
B8V	12500	4.0	0.44,0.557,1.0	#708eff	●
B8V	13000	4.0	0.436,0.554,1.0	#6f8dff	●
B7V	13500	4.0	0.432,0.55,1.0	#6e8cff	●
B7V	14000	4.0	0.429,0.547,1.0	#6d8bff	●
B6V	14500	4.0	0.425,0.544,1.0	#6c8aff	●
B6V	15000	4.0	0.421,0.541,1.0	#6b89ff	●
B5V	16000	4.0	0.414,0.536,1.0	#6988ff	●
B3V	17000	4.0	0.408,0.532,1.0	#6887ff	●
B2.5V	18000	4.0	0.403,0.527,1.0	#6686ff	●
B2.5V	19000	4.0	0.398,0.524,1.0	#6585ff	●
B2V	20000	4.0	0.394,0.52,1.0	#6484ff	●
B2V	21000	4.0	0.39,0.517,1.0	#6383ff	●
B2V	22000	4.0	0.387,0.514,1.0	#6283ff	●
B1.5V	23000	4.0	0.384,0.512,1.0	#6182ff	●
B1.5V	24000	4.0	0.381,0.509,1.0	#6181ff	●
B1.5V	25000	4.0	0.379,0.507,1.0	#6081ff	●
B1V	26000	4.0	0.376,0.505,1.0	#5f80ff	●
B1V	27000	4.0	0.373,0.503,1.0	#5f80ff	●
B1V	27500	4.0	0.371,0.501,1.0	#5e7fff	●
B0.5V	28000	4.0	0.371,0.5,1.0	#5e7fff	●
B0.5V	29000	4.0	0.368,0.498,1.0	#5d7fff	●
B0.5V	30000	4.0	0.366,0.496,1.0	#5d7eff	●
O9.5V	32500	4.0	0.361,0.491,1.0	#5c7dff	●
O8V	35000	4.0	0.357,0.487,1.0	#5b7cff	●
O6V	37500	4.0	0.359,0.487,1.0	#5b7cff	●
O5V	40000	4.0	0.358,0.486,1.0	#5b7bff	●
O4V	42500	4.0	0.357,0.485,1.0	#5a7bff	●
O4V	45000	4.0	0.357,0.485,1.0	#5a7bff	●
O3V	47500	4.0	0.357,0.485,1.0	#5b7bff	●
O2V	50000	4.0	0.358,0.486,1.0	#5b7bff	●
O2V	52500	4.0	0.359,0.487,1.0	#5b7cff	●
O1V	55000	4.0	0.361,0.489,1.0	#5c7cff	●

Bibliography

[1] Ejnar Hertzsprung. Ueber die Verwendung photographischer effektiver Wellen-laengen zur Bestimmung von Farbenaequivalenten. *Publikationen des Astro-physikalischen Observatoriums zu Potsdam*, 63, January 1911.

[2] Henry Norris Russell. Relations Between the Spectra and Other Characteristics of the Stars. *Popular Astronomy*, 22:275–294, May 1914.

[3] D. Pourbaix, Ž. Ivezić, G. R. Knapp, J. E. Gunn, and R. H. Lupton. Color-Induced Displacement double stars in SDSS. , 423:755–760, August 2004. doi: 10.1051/0004-6361:20040346.

[4] Roberto Sanchis-Ojeda, Daniel C. Fabrycky, Joshua N. Winn, Thomas Barclay, Bruce D. Clarke, Eric B. Ford, Jonathan J. Fortney, John C. Geary, Matthew J. Holman, Andrew W. Howard, Jon M. Jenkins, David Koch, Jack J. Lissauer, Geoffrey W. Marcy, Fergal Mullally, Darin Ragozzine, Shawn E. Seader, Martin Still, and Susan E. Thompson. Alignment of the stellar spin with the orbits of a three-planet system. , 487(7408):449–453, July 2012. doi: 10.1038/nature11301.

[5] Vincent Bourrier, Christophe Lovis, Hervé Beust, David Ehrenreich, Gregory W. Henry, Nicola Astudillo-Defru, Romain Allart, Xavier Bonfils, Damien Ségransan, Xavier Delfosse, Heather M. Cegla, Aurélien Wyttenbach, Kevin Heng, Baptiste Lavie, and Francesco Pepe. Orbital misalignment of the Neptune-mass exoplanet GJ 436b with the spin of its cool star. , 553(7689):477–480, January 2018. doi: 10.1038/nature24677.

[6] T.-O. Husser, S. Wende-von Berg, S. Dreizler, D. Homeier, A. Reiners, T. Barman, and P. H. Hauschildt. A new extensive library of PHOENIX stellar atmospheres and synthetic spectra. , 553:A6, May 2013. doi: 10.1051/0004-6361/201219058.

Bibliography

[7] P. H. Hauschildt and E. Baron. Numerical solution of the expanding stellar atmosphere problem. *Journal of Computational and Applied Mathematics*, 109 (1):41–63, September 1999.

[8] Thierry Lanz and Ivan Hubeny. A Grid of NLTE Line-blanketed Model Atmospheres of Early B-Type Stars. , 169(1):83–104, March 2007. doi: 10.1086/511270.

[9] Thierry Lanz and Ivan Hubeny. A Grid of Non-LTE Line-blanketed Model Atmospheres of O-Type Stars. , 146(2):417–441, June 2003. doi: 10.1086/ 374373.

[10] A. Stockman and L. Sharpe. Physiologically-based colour matching functions. *ISS/CIE Expert Symposium '06 "75 Years of the CIE Standard Colorimetric Observer"*, pages 13–20, 2008. URL `http://www.cvrl.org/people/Stockman/pubs/2006%20Physiological%20CMFs%20SS.pdf`.

[11] J.-V. Harre and René Heller. Color codes of stars. 2020.

[12] Mark J. Pecaut and Eric E. Mamajek. Intrinsic Colors, Temperatures, and Bolometric Corrections of Pre-main-sequence Stars. , 208(1):9, September 2013. doi: 10.1088/0067-0049/208/1/9.

[13] Z. Eker, V. Bakış, S. Bilir, F. Soydugan, I. Steer, E. Soydugan, H. Bakış, F. Aliçavuş, G. Aslan, and M. Alpsoy. Interrelated main-sequence mass-luminosity, mass-radius, and mass-effective temperature relations. , 479(4): 5491–5511, October 2018. doi: 10.1093/mnras/sty1834.

[14] A. Claret. Tables of Limb-darkening and Gravity-darkening Coefficients for the Space Mission Gaia. *Research Notes of the American Astronomical Society*, 3 (1):17, January 2019. doi: 10.3847/2515-5172/aaffdf.

[15] Michael Weiler. Revised Gaia Data Release 2 passbands. , 617:A138, October 2018. doi: 10.1051/0004-6361/201833462.

[16] René Heller. Analytic solutions to the maximum and average exoplanet transit depth for common stellar limb darkening laws. , 623:A137, March 2019. doi: 10.1051/0004-6361/201834620.

21

[17] Heinz Neckel and Dietrich Labs. Asymmetry and variations of solar limb darkening along the diameter defined by diurnal motion in April 1981. , 110(1): 139–170, March 1987. doi: 10.1007/BF00148209.

[18] Amy D. North and Mark D. Fairchild. Measuring color-matching functions. part ii. new data for assessing observer metamerism. *Color Research & Application*, 18(3):163–170, 1993. doi: 10.1002/col.5080180306. URL `https://onlinelibrary.wiley.com/doi/abs/10.1002/col.5080180306`.

[19] W. Schlosser, T. Schmidt-Kaler, and E. F. Milone. *Challenges of Astronomy. Hands-on Experiments for the Sky and Laboratory.* 1991.

[20] I. E. Gordon, L. S. Rothman, C. Hill, R. V. Kochanov, Y. Tan, P. F. Bernath, M. Birk, V. Boudon, A. Campargue, K. V. Chance, B. J. Drouin, J. M. Flaud, R. R. Gamache, J. T. Hodges, D. Jacquemart, V. I. Perevalov, A. Perrin, K. P. Shine, M. A. H. Smith, J. Tennyson, G. C. Toon, H. Tran, V. G. Tyuterev, A. Barbe, A. G. Császár, V. M. Devi, T. Furtenbacher, J. J. Harrison, J. M. Hartmann, A. Jolly, T. J. Johnson, T. Karman, I. Kleiner, A. A. Kyuberis, J. Loos, O. M. Lyulin, S. T. Massie, S. N. Mikhailenko, N. Moazzen-Ahmadi, H. S. P. Müller, O. V. Naumenko, A. V. Nikitin, O. L. Polyansky, M. Rey, M. Rotger, S. W. Sharpe, K. Sung, E. Starikova, S. A. Tashkun, J. Vand er Auwera, G. Wagner, J. Wilzewski, P. Wcisło, S. Yu, and E. J. Zak. The HITRAN2016 molecular spectroscopic database. , 203:3–69, December 2017. doi: 10.1016/j.jqsrt.2017.06.038.

[21] Jesse L. Greenstein. *The Spectra of the White Dwarfs*, pages 161–186. Springer Berlin Heidelberg, Berlin, Heidelberg, 1958. ISBN 978-3-642-45906-1. doi: 10.1007/978-3-642-45906-1_5. URL `https://doi.org/10.1007/978-3-642-45906-1_5`.

[22] G. Wegner and F. H. Yackovich. The cool DC white dwarf Stein 2051B. , 275: 240–246, December 1983. doi: 10.1086/161528.

[23] Andrew Vanderburg, Saul A. Rappaport, Siyi Xu, Ian J. M. Crossfield, Juliette C. Becker, Bruce Gary, Felipe Murgas, Simon Blouin, Thomas G. Kaye, Enric Palle, Carl Melis, Brett M. Morris, Laura Kreidberg, Varoujan Gorjian, Caroline V. Morley, Andrew W. Mann, Hannu Parviainen, Logan A. Pearce, Elisabeth R. Newton, Andreia Carrillo, Ben Zuckerman, Lorne Nelson, Greg

Bibliography

Zeimann, Warren R. Brown, René Tronsgaard, Beth Klein, George R. Ricker, Roland K. Vanderspek, David W. Latham, Sara Seager, Joshua N. Winn, Jon M. Jenkins, Fred C. Adams, Björn Benneke, David Berardo, Lars A. Buchhave, Douglas A. Caldwell, Jessie L. Christiansen, Karen A. Collins, Knicole D. Colón, Tansu Daylan, John Doty, Alexandra E. Doyle, Diana Dragomir, Courtney Dressing, Patrick Dufour, Akihiko Fukui, Ana Glidden, Natalia M. Guerrero, Xueying Guo, Kevin Heng, Andreea I. Henriksen, Chelsea X. Huang, Lisa Kaltenegger, Stephen R. Kane, John A. Lewis, Jack J. Lissauer, Farisa Morales, Norio Narita, Joshua Pepper, Mark E. Rose, Jeffrey C. Smith, Keivan G. Stassun, and Liang Yu. A giant planet candidate transiting a white dwarf. *Nature*, 585(7825):363–367, 2020. doi: 10.1038/s41586-020-2713-y. URL https://doi.org/10.1038/s41586-020-2713-y.